






Image-Based Visual Servoing for Enhanced Cooperation of Dual-Arm Manipulation

Zizhe Zhang , Yuan Yang , *Member, IEEE*, Wenqiang Zuo, Guangming Song , *Senior Member, IEEE*, Aiguo Song , *Senior Member, IEEE*, Yang Shi , *Fellow, IEEE*

Abstract—The cooperation of a pair of robot manipulators is required to manipulate a target object without any fixtures. The conventional control methods coordinate the end-effector pose of each manipulator with that of the other using their kinematics and joint coordinate measurements. Yet, the manipulators' inaccurate kinematics and joint coordinate measurements can cause significant pose synchronization errors in practice. This paper thus proposes an image-based visual servoing approach for enhancing the cooperation of a dual-arm manipulation system. On top of the classical control, the visual servoing controller lets each manipulator use its carried camera to measure the image features of the other's marker and adapt its end-effector pose with the counterpart on the move. Because visual measurements are robust to kinematic errors, the proposed control can reduce the end-effector pose synchronization errors and the fluctuations of the interaction forces of the pair of manipulators on the move. Theoretical analyses have rigorously proven the stability of the closed-loop system. Comparative experiments on real robots have substantiated the effectiveness of the proposed control.

Index Terms—Cooperative manipulation, image-based visual servoing, multirobot systems, passivity-based control.

I. INTRODUCTION

Dual-arm manipulation remains a challenging and largely underdeveloped field in the robotics society [1]. Given that typical humanoid robots have bimanual capabilities, the study of dual-arm manipulation control is gaining more and more attention recently [2]. A typical application of dual-arm manipulation is to grasp and transport a rigid target object without extra fixtures [3]. In this context, the two arms need to keep their end effectors in frictional contact with the manipulated object throughout the task execution [4]. Thus, a fundamental control objective for the pair of two manipulators is to tightly coordinate their end-effector poses on the move [5].

The existing research on dual-arm manipulation control has synchronized the end-effector positions of both manipulators with event-triggered communications [6] and regulated their interaction forces with the object in the contact direction [7]. Accounting for the internal forces [8], constrained quadratic

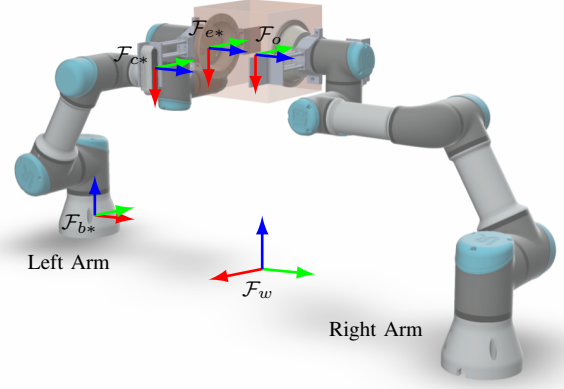


Figure 1. Two 6-DOF serial manipulators serve as the left and the right arms in a dual-arm manipulation system. The target object that they manipulate is a cubic box. \mathcal{F}_w and \mathcal{F}_o denote the world frame and the object frame, respectively. \mathcal{F}_{b*} , \mathcal{F}_{e*} and \mathcal{F}_{c*} are the base, end-effector and camera frames of the left $*$ = l and the right $*$ = r arms.

programs have been formulated to minimize the contact forces while avoiding obstacles in the surrounding environment [9] and the separation or sliding of the frictional contact [10]. Under nonlinear model predictive control, a torque-controlled dual-arm manipulation system has recently been tested for a mirror grinding task [11]. However, torque-controlled manipulators with exactly known dynamic models are unavailable in many applications. Cooperation approaches for velocity- and position-controlled robot arms have thus been advocated. For velocity-controlled manipulators, the joint limit avoidance and Cartesian-space path following have been pursued with lower priority than their pose synchronization task [12]. A sparse kinematic control has minimized the number of the two arms' actuated joints using a hierarchical quadratic program [13]. For position-controlled manipulators, a linear elastic model for the contact of the follower arm with the object has been assumed to minimize the internal forces [14]. A communication-free coordination control has adopted the manipulators' interaction forces to transport deformable objects [15].

A position-based visual servoing (PBVS) approach has been deployed on a humanoid robot to control both arms/hands to grasp and manipulate its observed target objects in a kitchen environment [16]. An image-based visual servoing (IBVS) method has been applied to a dual-arm robot with both fixed and mobile cameras to align the poses of both arms when performing a plug-socket insertion task [17]. Yet, the control design and stability analysis have not considered the closed

Zizhe Zhang is with the Department of Electrical and System Engineering, University of Pennsylvania, Philadelphia, PA 19104, United States (e-mail: zizhez@seas.upenn.edu).

Yuan Yang, Guangming Song and Aiguo Song are with the School of Instrument Science and Engineering, Southeast University, Nanjing, Jiangsu 210096, China (e-mail: yuan_evan_yang@seu.edu.cn; mikesong@seu.edu.cn; a.g.song@seu.edu.cn).

Wenqiang Zuo is with the School of Materials Science and Engineering, Southeast University, Nanjing, Jiangsu 211189, China (e-mail: wenqiangzuo@seu.edu.cn).

Yang Shi is with the Department of Mechanical Engineering, University of Victoria, Victoria, BC V8W 2Y2, Canada (e-mail: yshi@uvic.ca).

kinematic chain. With IBVS, two simulated aerial manipulators have rigidly grasped an assembly bar and transported it to the target pose [18]. However, the control has not yet been verified on any real-robot platform.

Unlike the above-reviewed research results, this paper enhances the cooperation of dual-arm manipulation by IBVS with explicit consideration of the closed-chain kinematics and real-robot experimental validations. The classical controls have distributed the cooperative manipulation task to both manipulators as their motion references [19] and have synchronized the poses of both manipulators using their kinematics and joint measurements [20]. Nevertheless, in the presence of kinematic errors, each manipulator coordinates the biased pose of its end effector with the biased pose of the other's end effector. As a result, the dual-arm robot changes the relative poses of its two end effectors during the movement, possibly leading to task failures and hardware damage. An adaptive controller has handled the manipulators' uncertain kinematic parameters by recursive least-squares estimators [21]. Yet, the joint coordinate measurement errors have not been addressed. Because IBVS is robust to the manipulators' kinematic errors [22], this paper tailors IBVS to dual-arm manipulation by modeling the kinematics of both arms and their wrist-mounted cameras, deriving the associated interaction matrix of the entire system, and synthesizing the visual servoing controls with the conventional controls [19], [20]. The paper has also proven the stability of the closed-loop system and interpreted the cooperation enhancement by IBVS. Comparative experiments with the classical controls [19], [20] on a real-robot platform have verified the effectiveness of the proposed control.

II. MODELING

This section introduces the closed kinematic chain formed by the pair of manipulators and the pinhole perspective projection model of their wrist-mounted cameras.

A. The Closed Kinematic Chain

The dual-arm manipulation system, as shown in Figure 1, contains a pair of 6-degrees-of-freedom (6-DOF) serial manipulators with only revolute joints. Let the world frame be \mathcal{F}_w , the base and the end-effector frames of the left $* = l$ and the right $* = r$ arms be \mathcal{F}_{b*} and \mathcal{F}_{e*} , respectively. Let \mathbf{q}_* be the joint coordinates and

$$\mathbf{T}_* = \begin{bmatrix} \mathbf{R}_* & \mathbf{x}_* \\ \mathbf{0} & 1 \end{bmatrix}$$

be the end-effector poses of the two arms $* = l, r$, where \mathbf{R}_* and \mathbf{x}_* are the rotation matrix representations of orientation and the positions respectively. The Jacobian matrices $\mathbf{J}_*(\mathbf{q}_*)$ of the two manipulators $* = l, r$ then link their joint velocity inputs $\dot{\mathbf{q}}_*$ to their end-effector velocities \mathbf{v}_* by

$$\mathbf{v}_* = \begin{bmatrix} \mathbf{v}_* \\ \boldsymbol{\omega}_* \end{bmatrix} = \mathbf{J}_*(\mathbf{q}_*)\dot{\mathbf{q}}_*, \quad (1)$$

where the linear \mathbf{v}_* and angular $\boldsymbol{\omega}_*$ velocities adapt their end-effector poses \mathbf{T}_* by

$$\dot{\mathbf{x}}_* = \mathbf{v}_*, \quad (2a)$$

$$\dot{\mathbf{R}}_* = \boldsymbol{\omega}_*^\times \mathbf{R}_*. \quad (2b)$$

To manipulate the target object without fixtures, the two manipulators need to keep their end effectors rigidly attached to the object throughout the task execution. Let \mathcal{F}_o be the object frame, and let \mathbf{T}_o be the object pose. Then, the rigid attachment of the arms' end effectors to the object requires

$$\mathbf{T}_l \mathbf{T}_o^l = \mathbf{T}_o = \mathbf{T}_r \mathbf{T}_o^r, \quad (3)$$

where the poses of the object relative to the end effectors of the left \mathbf{T}_o^l and the right \mathbf{T}_o^r arms remain invariant. Simple algebraic operations derive that the transformations

$$\mathbf{T}_r^l = \mathbf{T}_l^{-1} \mathbf{T}_r = \mathbf{T}_o^l \mathbf{T}_o^{r-1}, \quad (4a)$$

$$\mathbf{T}_l^r = \mathbf{T}_r^{-1} \mathbf{T}_l = \mathbf{T}_o^r \mathbf{T}_o^{l-1} \quad (4b)$$

remain invariant. Namely, the end effectors of the two manipulators stay relatively stationary. Let

$$\bar{\mathbf{T}}_* = \begin{bmatrix} \bar{\mathbf{R}}_* & \bar{\mathbf{x}}_* \\ \mathbf{0} & 1 \end{bmatrix}$$

denote the initial end-effector poses of the left $* = l$ and the right $* = r$ manipulators. The pose synchronization control objective of the dual-arm system can thus be formulated as

$$\bar{\mathbf{T}}_l^{-1} \mathbf{T}_l = \bar{\mathbf{T}}_r^{-1} \mathbf{T}_r. \quad (5)$$

B. The Pinhole Projection Model

The eye-in-hand camera mounted on the wrist of each manipulator, as shown in Figure 1, measures the image features of the fiducial marker fixed on the wrist of the other manipulator. In particular, the image features adopted in the control design are the four corner points of each AprilTag marker. Let the pose of the camera frame \mathcal{F}_{c*} relative to the end-effector frame \mathcal{F}_{e*} of the left $* = l$ or the right $* = r$ arm be

$$\mathbf{T}_c^* = \begin{bmatrix} \mathbf{R}_c^* & \mathbf{x}_c^* \\ \mathbf{0} & 1 \end{bmatrix}.$$

Let the position of the i -th corner point of the marker on the right $* = r$ or the left $* = l$ arm be expressed in the end-effector frame \mathcal{F}_* by \mathbf{p}_{*i} with $i = 1, 2, 3, 4$.

By the kinematic chain, the position $\mathbf{m}_{li} = (m_{li}^x, m_{li}^y, m_{li}^z)^\top$ of the i -th corner point of the right arm's marker expressed in the left arm's camera frame \mathcal{F}_{cl} meets

$$\mathbf{T}_l \mathbf{T}_c^l \begin{bmatrix} \mathbf{m}_{li} \\ 1 \end{bmatrix} = \mathbf{T}_r \begin{bmatrix} \mathbf{p}_{ri} \\ 1 \end{bmatrix}.$$

The position $\mathbf{m}_{ri} = (m_{ri}^x, m_{ri}^y, m_{ri}^z)^\top$ of the i -th corner point of the left arm's marker expressed in the right arm's camera frame \mathcal{F}_r meets

$$\mathbf{T}_r \mathbf{T}_c^r \begin{bmatrix} \mathbf{m}_{ri} \\ 1 \end{bmatrix} = \mathbf{T}_l \begin{bmatrix} \mathbf{p}_{li} \\ 1 \end{bmatrix}.$$

One can thus derive that

$$\mathbf{m}_{li} = (\mathbf{R}_l \mathbf{R}_c^l)^\top (\mathbf{R}_r \mathbf{p}_{ri} + \mathbf{x}_r - \mathbf{R}_l \mathbf{x}_c^l - \mathbf{x}_l), \quad (6a)$$

$$\mathbf{m}_{ri} = (\mathbf{R}_r \mathbf{R}_c^r)^\top (\mathbf{R}_l \mathbf{p}_{li} + \mathbf{x}_l - \mathbf{R}_r \mathbf{x}_c^r - \mathbf{x}_r), \quad (6b)$$

for the corner points $i = 1, 2, 3, 4$ of markers.

Let ζ_{*i} normalize \mathbf{m}_{*i} with $* = l, r$ by their z -coordinates

$$\zeta_{*i} = \begin{bmatrix} \frac{m_{*i}^x}{m_{*i}^z} & \frac{m_{*i}^y}{m_{*i}^z} \end{bmatrix}^\top.$$

Let the intrinsic parameters matrices of the left $* = l$ and the right $* = r$ cameras be \mathbf{K}_* . The cameras then capture their image features \mathbf{s}_{*i} with $i = 1, 2, 3, 4$ by

$$\mathbf{s}_{*i} = \mathbf{K}_* \zeta_{*i}. \quad (7)$$

Taking the time derivative of Equation (7) yields

$$\dot{\mathbf{s}}_{*i} = \frac{1}{m_{*i}^z} [\mathbf{K}_* \quad -\mathbf{s}_{*i}] \dot{\mathbf{m}}_{*i}. \quad (8)$$

Substituting Equation (6) into Equation (8) gives rise to

$$\begin{bmatrix} \dot{\mathbf{s}}_{li} \\ \dot{\mathbf{s}}_{ri} \end{bmatrix} = \begin{bmatrix} \mathbf{L}_{li}^l & \mathbf{L}_{li}^r \\ \mathbf{L}_{ri}^l & \mathbf{L}_{ri}^r \end{bmatrix} \begin{bmatrix} \mathbf{v}_l \\ \mathbf{v}_r \end{bmatrix}, \quad (9)$$

where the interaction matrices \mathbf{L}_{li}^l , \mathbf{L}_{li}^r , \mathbf{L}_{ri}^l and \mathbf{L}_{ri}^r with $i = 1, 2, 3, 4$ are expressed as

$$\begin{aligned} \mathbf{L}_{li}^l &= \frac{1}{m_{li}^z} [\mathbf{K}_l \quad -\mathbf{s}_{li}] (\mathbf{R}_l \mathbf{R}_c^l)^T [-\mathbf{I} \quad (\mathbf{R}_r \mathbf{p}_{ri} + \mathbf{x}_r - \mathbf{x}_l)^\times], \\ \mathbf{L}_{li}^r &= \frac{1}{m_{li}^z} [\mathbf{K}_l \quad -\mathbf{s}_{li}] (\mathbf{R}_l \mathbf{R}_c^l)^T [\mathbf{I} \quad -(\mathbf{R}_r \mathbf{p}_{ri})^\times], \\ \mathbf{L}_{ri}^l &= \frac{1}{m_{ri}^z} [\mathbf{K}_r \quad -\mathbf{s}_{ri}] (\mathbf{R}_r \mathbf{R}_c^r)^T [\mathbf{I} \quad -(\mathbf{R}_l \mathbf{p}_{li})^\times], \\ \mathbf{L}_{ri}^r &= \frac{1}{m_{ri}^z} [\mathbf{K}_r \quad -\mathbf{s}_{ri}] (\mathbf{R}_r \mathbf{R}_c^r)^T [-\mathbf{I} \quad (\mathbf{R}_l \mathbf{p}_{li} + \mathbf{x}_l - \mathbf{x}_r)^\times]. \end{aligned}$$

Let $\bar{\mathbf{s}}_{li}$ and $\bar{\mathbf{s}}_{ri}$ be the initial values of \mathbf{s}_{li} and \mathbf{s}_{ri} , respectively. The enhanced cooperation control objective of the dual-arm system can thus be formulated as

$$\begin{bmatrix} \mathbf{s}_{li} \\ \mathbf{s}_{ri} \end{bmatrix} = \begin{bmatrix} \bar{\mathbf{s}}_{li} \\ \bar{\mathbf{s}}_{ri} \end{bmatrix} \quad (10)$$

for the corner points $i = 1, 2, 3, 4$ of markers.

III. CONTROL DESIGN AND STABILITY ANALYSIS

This section designs the control inputs to the manipulators and analyzes the stability of the closed-loop system.

A. Control Design

The control objective (5) can be described in detail by

$$\bar{\mathbf{T}}_l^{-1} \mathbf{T}_l = \begin{bmatrix} \tilde{\mathbf{R}}_l & \tilde{\mathbf{R}}_l^T \tilde{\mathbf{x}}_l \\ \mathbf{0} & 1 \end{bmatrix} = \begin{bmatrix} \tilde{\mathbf{R}}_r & \tilde{\mathbf{R}}_r^T \tilde{\mathbf{x}}_r \\ \mathbf{0} & 1 \end{bmatrix} = \bar{\mathbf{T}}_r^{-1} \mathbf{T}_r,$$

where $\tilde{\mathbf{R}}_* = \bar{\mathbf{R}}_*^T \mathbf{R}_*$ and $\tilde{\mathbf{x}}_* = \mathbf{x}_* - \bar{\mathbf{x}}_*$ for $* = l, r$. Namely,

$$\begin{aligned} \mathbf{I} &= \tilde{\mathbf{R}}_l \tilde{\mathbf{R}}_r^T, \\ \mathbf{0} &= \bar{\mathbf{R}}_l^T \tilde{\mathbf{x}}_l - \bar{\mathbf{R}}_r^T \tilde{\mathbf{x}}_r. \end{aligned}$$

The pose synchronization control can thus be reformulated as an optimization problem as follows

$$\underset{\mathbf{q}_l, \mathbf{q}_r}{\text{minimize}} \quad V_t, \quad (11)$$

where the objective function is defined by

$$V_t = \frac{1}{2} \text{tr}(\mathbf{I} - \tilde{\mathbf{R}}_l \tilde{\mathbf{R}}_r^T) + \frac{1}{2} (\bar{\mathbf{R}}_l^T \tilde{\mathbf{x}}_l - \bar{\mathbf{R}}_r^T \tilde{\mathbf{x}}_r)^T (\bar{\mathbf{R}}_l^T \tilde{\mathbf{x}}_l - \bar{\mathbf{R}}_r^T \tilde{\mathbf{x}}_r)$$

with $\text{tr}(\mathbf{M})$ being the trace of any square matrix \mathbf{M} . Likely, the enhanced cooperation control objective (10) can be reformulated as the following optimization problem

$$\underset{\mathbf{q}_l, \mathbf{q}_r}{\text{minimize}} \quad V_s, \quad (12)$$

where the objective function is defined by

$$V_s = \frac{1}{2} \sum_{i=1}^4 [(\mathbf{s}_{li} - \bar{\mathbf{s}}_{li})^T (\mathbf{s}_{li} - \bar{\mathbf{s}}_{li}) + (\mathbf{s}_{ri} - \bar{\mathbf{s}}_{ri})^T (\mathbf{s}_{ri} - \bar{\mathbf{s}}_{ri})].$$

Therefore, IBVS for enhancing the cooperation of dual-arm manipulation is formulated as solving the optimization problems (11) and (12) simultaneously by

$$\underset{\mathbf{q}_l, \mathbf{q}_r}{\text{minimize}} \quad V = w_t V_t + w_s V_s, \quad (13)$$

where the objective function V sums the objective functions V_t and V_s by positive scalar weights w_t and w_s , respectively.

Following the steepest descent algorithm, the joint velocity control inputs to the left and the right arms are designed by

$$\begin{aligned} \dot{\mathbf{q}}_l &= -w_s \mathbf{J}_l(\mathbf{q}_l)^T \sum_{i=1}^4 [\mathbf{L}_{li}^l{}^T (\mathbf{s}_{li} - \bar{\mathbf{s}}_{li}) + \mathbf{L}_{ri}^l{}^T (\mathbf{s}_{ri} - \bar{\mathbf{s}}_{ri})] \\ &\quad - w_t \mathbf{J}_l(\mathbf{q}_l)^T \left[\begin{array}{c} \tilde{\mathbf{x}}_l - \bar{\mathbf{R}}_l \bar{\mathbf{R}}_r^T \tilde{\mathbf{x}}_r \\ \text{sk}(\bar{\mathbf{R}}_l \tilde{\mathbf{R}}_r^T \bar{\mathbf{R}}_l^T)^\vee \end{array} \right], \end{aligned} \quad (14a)$$

$$\begin{aligned} \dot{\mathbf{q}}_r &= -w_s \mathbf{J}_r(\mathbf{q}_r)^T \sum_{i=1}^4 [\mathbf{L}_{li}^r{}^T (\mathbf{s}_{li} - \bar{\mathbf{s}}_{li}) + \mathbf{L}_{ri}^r{}^T (\mathbf{s}_{ri} - \bar{\mathbf{s}}_{ri})] \\ &\quad - w_t \mathbf{J}_r(\mathbf{q}_r)^T \left[\begin{array}{c} \tilde{\mathbf{x}}_r - \bar{\mathbf{R}}_r \bar{\mathbf{R}}_l^T \tilde{\mathbf{x}}_l \\ \text{sk}(\bar{\mathbf{R}}_r \tilde{\mathbf{R}}_l^T \bar{\mathbf{R}}_r^T)^\vee \end{array} \right], \end{aligned} \quad (14b)$$

where $\dot{\mathbf{q}}_l$ and $\dot{\mathbf{q}}_r$ are respectively the negative gradients of the objective function V with respect to \mathbf{q}_l and \mathbf{q}_r , and $\text{sk}(\mathbf{M})^\vee$ returns the vector associated with the skew-symmetric part of any square matrix \mathbf{M} . It is exposed in the next subsection to prove the closed-loop stability.

B. Stability Analysis

One can investigate the stability of the closed-loop dual-arm manipulation system by the objective function V defined in Equation (13). Under the joint velocity control inputs (14), the kinematics (1) and (2) of the left and the right manipulators adapt the objective function V by

$$\dot{V} = w_t \dot{V}_t + w_s \dot{V}_s = -\dot{\mathbf{q}}_l^T \dot{\mathbf{q}}_l - \dot{\mathbf{q}}_r^T \dot{\mathbf{q}}_r \leq 0, \quad (15)$$

where the time derivatives of V_t and V_s are presented in detail in (16) and (17), respectively. Because the objective function V is nonnegative and its time derivative is nonpositive, one can thus conclude that the states \mathbf{q}_l and \mathbf{q}_r of the system converge to the largest invariant set of

$$\{(\mathbf{q}_l, \mathbf{q}_r) \mid \dot{\mathbf{q}}_l = \dot{\mathbf{q}}_r = \mathbf{0}\}$$

by LaSalle's invariance principle. That is, both arms become stationary asymptotically.

From Equations (16) and (17), one can find that the joint velocity control inputs $\dot{\mathbf{q}}_l$ and $\dot{\mathbf{q}}_r$ of the left and the right arms designed in (14) can be written as

$$\dot{\mathbf{q}}_l = -w_s \nabla_{\mathbf{q}_l} V_s - w_t \nabla_{\mathbf{q}_l} V_t, \quad (18a)$$

$$\dot{\mathbf{q}}_r = -w_s \nabla_{\mathbf{q}_r} V_s - w_t \nabla_{\mathbf{q}_r} V_t, \quad (18b)$$

where $\nabla_{\mathbf{q}_*} V_t$ and $\nabla_{\mathbf{q}_*} V_s$ are the gradients of the objective functions V_t and V_s with respect to \mathbf{q}_* for $* = l, r$. Then, the

$$\begin{aligned}
\dot{V}_t &= -\frac{1}{2}\text{tr}\left(\dot{\tilde{\mathbf{R}}}_l\tilde{\mathbf{R}}_r^\top + \tilde{\mathbf{R}}_l\dot{\tilde{\mathbf{R}}}_r^\top\right) + (\overline{\mathbf{R}}_l^\top\tilde{\mathbf{x}}_l - \overline{\mathbf{R}}_r^\top\tilde{\mathbf{x}}_r)^\top (\overline{\mathbf{R}}_l^\top\dot{\tilde{\mathbf{x}}}_l - \overline{\mathbf{R}}_r^\top\dot{\tilde{\mathbf{x}}}_r) \\
&= -\frac{1}{2}\text{tr}\left(\overline{\mathbf{R}}_l^\top\dot{\tilde{\mathbf{R}}}_l\tilde{\mathbf{R}}_r^\top + \tilde{\mathbf{R}}_l\dot{\tilde{\mathbf{R}}}_r^\top\overline{\mathbf{R}}_r\right) + (\overline{\mathbf{R}}_l^\top\tilde{\mathbf{x}}_l - \overline{\mathbf{R}}_r^\top\tilde{\mathbf{x}}_r)^\top (\overline{\mathbf{R}}_l^\top\dot{\tilde{\mathbf{x}}}_l - \overline{\mathbf{R}}_r^\top\dot{\tilde{\mathbf{x}}}_r) \\
&= -\frac{1}{2}\text{tr}\left(\dot{\tilde{\mathbf{R}}}_l\tilde{\mathbf{R}}_r^\top\overline{\mathbf{R}}_l^\top\right) - \frac{1}{2}\text{tr}\left(\overline{\mathbf{R}}_r\tilde{\mathbf{R}}_l\dot{\tilde{\mathbf{R}}}_r^\top\right) + (\overline{\mathbf{R}}_l^\top\tilde{\mathbf{x}}_l - \overline{\mathbf{R}}_r^\top\tilde{\mathbf{x}}_r)^\top \overline{\mathbf{R}}_l^\top\dot{\tilde{\mathbf{x}}}_l + (\overline{\mathbf{R}}_r^\top\tilde{\mathbf{x}}_r - \overline{\mathbf{R}}_l^\top\tilde{\mathbf{x}}_l)^\top \overline{\mathbf{R}}_r^\top\dot{\tilde{\mathbf{x}}}_r \\
&= -\frac{1}{2}\text{tr}\left(\omega_l^\times\tilde{\mathbf{R}}_l\tilde{\mathbf{R}}_r^\top\overline{\mathbf{R}}_l^\top\right) + \frac{1}{2}\text{tr}\left(\overline{\mathbf{R}}_r\tilde{\mathbf{R}}_l\tilde{\mathbf{R}}_r^\top\omega_r^\times\right) + (\overline{\mathbf{R}}_l^\top\tilde{\mathbf{x}}_l - \overline{\mathbf{R}}_r^\top\tilde{\mathbf{x}}_r)^\top \overline{\mathbf{R}}_l^\top\mathbf{v}_l + (\overline{\mathbf{R}}_r^\top\tilde{\mathbf{x}}_r - \overline{\mathbf{R}}_l^\top\tilde{\mathbf{x}}_l)^\top \overline{\mathbf{R}}_r^\top\mathbf{v}_r \\
&= \omega_l^\top\text{sk}\left(\tilde{\mathbf{R}}_l\tilde{\mathbf{R}}_r^\top\overline{\mathbf{R}}_l^\top\right)^\vee + \omega_r^\top\text{sk}\left(\overline{\mathbf{R}}_r\tilde{\mathbf{R}}_l\tilde{\mathbf{R}}_r^\top\right)^\vee + (\tilde{\mathbf{x}}_l - \overline{\mathbf{R}}_l\overline{\mathbf{R}}_r^\top\tilde{\mathbf{x}}_r)^\top \mathbf{v}_l + (\tilde{\mathbf{x}}_r - \overline{\mathbf{R}}_r\overline{\mathbf{R}}_l^\top\tilde{\mathbf{x}}_l)^\top \mathbf{v}_r \\
&= \begin{bmatrix} \tilde{\mathbf{x}}_l - \overline{\mathbf{R}}_l\overline{\mathbf{R}}_r^\top\tilde{\mathbf{x}}_r \\ \text{sk}\left(\tilde{\mathbf{R}}_l\tilde{\mathbf{R}}_r^\top\overline{\mathbf{R}}_l^\top\right)^\vee \end{bmatrix}^\top \mathbf{v}_l + \begin{bmatrix} \tilde{\mathbf{x}}_r - \overline{\mathbf{R}}_r\overline{\mathbf{R}}_l^\top\tilde{\mathbf{x}}_l \\ \text{sk}\left(\overline{\mathbf{R}}_r\tilde{\mathbf{R}}_l\tilde{\mathbf{R}}_r^\top\right)^\vee \end{bmatrix}^\top \mathbf{v}_r = \begin{bmatrix} \nabla_{\mathbf{q}_l} V_t \\ \nabla_{\mathbf{q}_r} V_t \end{bmatrix}^\top \begin{bmatrix} \dot{\mathbf{q}}_l \\ \dot{\mathbf{q}}_r \end{bmatrix}
\end{aligned} \tag{16}$$

$$\begin{aligned}
\dot{V}_s &= \sum_{i=1}^4 \begin{bmatrix} \mathbf{s}_{li} - \bar{\mathbf{s}}_{li} \\ \mathbf{s}_{ri} - \bar{\mathbf{s}}_{ri} \end{bmatrix}^\top \begin{bmatrix} \dot{\mathbf{s}}_{li} \\ \dot{\mathbf{s}}_{ri} \end{bmatrix} = \sum_{i=1}^4 \begin{bmatrix} \mathbf{s}_{li} - \bar{\mathbf{s}}_{li} \\ \mathbf{s}_{ri} - \bar{\mathbf{s}}_{ri} \end{bmatrix}^\top \begin{bmatrix} \mathbf{L}_{li}^l & \mathbf{L}_{ri}^r \\ \mathbf{L}_{li}^r & \mathbf{L}_{ri}^r \end{bmatrix} \begin{bmatrix} \mathbf{v}_l \\ \mathbf{v}_r \end{bmatrix} = \sum_{i=1}^4 \left(\begin{bmatrix} \mathbf{L}_{li}^l & \mathbf{L}_{ri}^r \\ \mathbf{L}_{li}^r & \mathbf{L}_{ri}^r \end{bmatrix}^\top \begin{bmatrix} \mathbf{s}_{li} - \bar{\mathbf{s}}_{li} \\ \mathbf{s}_{ri} - \bar{\mathbf{s}}_{ri} \end{bmatrix} \right)^\top \begin{bmatrix} \mathbf{v}_l \\ \mathbf{v}_r \end{bmatrix} \\
&= \sum_{i=1}^4 \begin{bmatrix} \mathbf{L}_{li}^l{}^\top (\mathbf{s}_{li} - \bar{\mathbf{s}}_{li}) + \mathbf{L}_{ri}^l{}^\top (\mathbf{s}_{ri} - \bar{\mathbf{s}}_{ri}) \\ \mathbf{L}_{li}^r{}^\top (\mathbf{s}_{li} - \bar{\mathbf{s}}_{li}) + \mathbf{L}_{ri}^r{}^\top (\mathbf{s}_{ri} - \bar{\mathbf{s}}_{ri}) \end{bmatrix}^\top \begin{bmatrix} \mathbf{v}_l \\ \mathbf{v}_r \end{bmatrix} = \begin{bmatrix} \nabla_{\mathbf{q}_l} V_s \\ \nabla_{\mathbf{q}_r} V_s \end{bmatrix}^\top \begin{bmatrix} \dot{\mathbf{q}}_l \\ \dot{\mathbf{q}}_r \end{bmatrix}
\end{aligned} \tag{17}$$

fact that $\dot{\mathbf{q}}_* \rightarrow \mathbf{0}$ together with (18) imply that the gradient of the objective function V tends to zero, i.e.,

$$\begin{bmatrix} \dot{\mathbf{q}}_l \\ \dot{\mathbf{q}}_r \end{bmatrix} = - \begin{bmatrix} \nabla_{\mathbf{q}_l} V \\ \nabla_{\mathbf{q}_r} V \end{bmatrix} = -\nabla V \rightarrow \mathbf{0}$$

as time goes to infinity, where $\nabla_{\mathbf{q}_*} V$ are the gradients of the objective function V with respect to \mathbf{q}_* . One can thus conclude that the objective function V converges to its minimum.

Note that the objective function V is not necessarily globally strictly convex with respect to \mathbf{q}_l and \mathbf{q}_r . The steady-state configuration of the dual-arm system can possibly be a local minimum point of V . Nevertheless, $V = 0$ at the initial time is exactly its global minimum by its definition, which implies that the proposed controls (14) reduce V back to zero asymptotically once it diverges a bit from zero throughout the cooperative manipulation. Therefore, both the pose synchronization control (5) and the enhanced cooperation control (10) objectives are fulfilled.

IV. DISCUSSION

This section discusses the pose synchronization errors at the steady state and the handling of state and input constraints for the dual-arm manipulation system.

A. Steady-State Pose Errors

The conventional controls coordinate the end-effector poses of the left $* = l$ and the right $* = r$ arms based upon their pose measurements. In the presence of the pose measurement errors, the joint velocity inputs to the two manipulators under the conventional controls turn to

$$\dot{\mathbf{q}}_* = -w_t \nabla_{\mathbf{q}_*} V_t + w_t \delta_*,$$

where the mismatched inputs δ_* are induced by the errors of the two arms' pose measurements. At the steady state, the manipulators become stationary, i.e., $\dot{\mathbf{q}}_* = \mathbf{0}$ and thence

$\nabla_{\mathbf{q}_*} V_t = \delta_* \neq \mathbf{0}$, which indicates the pose errors between the two manipulators.

By contrast, the joint velocity inputs to the two manipulators under the proposed control with pose measurement errors are

$$\dot{\mathbf{q}}_* = -w_s \nabla_{\mathbf{q}_*} V_s - w_t \nabla_{\mathbf{q}_*} V_t + w_t \delta_*.$$

Because the end-effector pose errors between the left $* = l$ and the right $* = r$ arms remain relatively small throughout the task execution, the gradients of the objective functions V_s and V_t are almost aligned, i.e., $\nabla_{\mathbf{q}_*} V_s \approx \alpha \nabla_{\mathbf{q}_*} V_t$ for some $\alpha > 0$. At the steady state, the arms become stationary, i.e., $w_s \nabla_{\mathbf{q}_*} V_s + w_t \nabla_{\mathbf{q}_*} V_t \approx (\alpha w_s + w_t) \nabla_{\mathbf{q}_*} V_t = w_t \delta_*$ and thence $\nabla_{\mathbf{q}_*} V_t \approx \frac{w_t}{\alpha w_s + w_t} \delta_*$. It confirms that the IBVS control does enhance the cooperation of the two manipulators by reducing their end-effector pose errors.

As a matter of fact, the conventional control and the IBVS control complement each other in the proposed control (14). Being robust to kinematic errors, the IBVS control improves the accuracy of the two manipulators' pose synchronization. However, the IBVS control suffers from its limited domain of attraction. The conventional control tackles the problem by confining the pose errors between the two arms' end effectors to the domain of attraction of the IBVS control. For this reason, the proposed control synthesizes the IBVS control with the conventional control rather than relying on the IBVS control individually.

B. State and Input Constraints

Implementing the proposed control on a real-robot platform needs to cope with the system's state and input constraints. For the velocity-controlled manipulators $* = l, r$, their joint angles \mathbf{q}_* and velocities $\dot{\mathbf{q}}_*$ are the states and inputs of the system, respectively. Typical state constraints of the velocity-control manipulators are imposed to avoid the mechanical limits of their joints, obstacles in the surrounding environment,

and collisions between their bodies. Together, all these state constraints can be unified into an inequality of the manipulators' joint angles as follows

$$h(\mathbf{q}_l, \mathbf{q}_r) \leq 0.$$

The input constraints are imposed to accommodate the limits of the left $* = l$ and the right $* = r$ arms' joint velocities. Namely, the joint velocity control inputs $\dot{\mathbf{q}}_*$ cannot exceed their maximum $\dot{\mathbf{q}}_*^{\max}$ and the minimum $\dot{\mathbf{q}}_*^{\min}$ values as follows

$$\dot{\mathbf{q}}_*^{\min} \leq \dot{\mathbf{q}}_* \leq \dot{\mathbf{q}}_*^{\max}.$$

Under the state constraints, the joint velocity control inputs to the manipulators can be designed by solving the optimization problem (13) with the penalty function

$$\psi(\mathbf{q}_l, \mathbf{q}_r) = \exp\left[\frac{\bar{h} - h(\mathbf{q}_l, \mathbf{q}_r)}{h(\mathbf{q}_l, \mathbf{q}_r)}\right] - \frac{\bar{h} - h(\mathbf{q}_l, \mathbf{q}_r)}{h(\mathbf{q}_l, \mathbf{q}_r)} - 1$$

for $\bar{h} < h(\mathbf{q}_l, \mathbf{q}_r) < 0$ and $\psi(\mathbf{q}_l, \mathbf{q}_r) = 0$ for $h(\mathbf{q}_l, \mathbf{q}_r) \leq \bar{h}$ with $\bar{h} < 0$. Then, the input constraints are guaranteed by scaling the velocity inputs $\dot{\mathbf{q}}_*$ with factors

$$\alpha_* = \max_{i=1, \dots, 6} \left(\frac{\dot{q}_{*i}}{\dot{q}_{*i}^{\max}}, \frac{\dot{q}_{*i}}{\dot{q}_{*i}^{\min}}, 1 \right),$$

where \dot{q}_{*i} , \dot{q}_{*i}^{\max} and \dot{q}_{*i}^{\min} are the i -th elements of $\dot{\mathbf{q}}_*$, $\dot{\mathbf{q}}_*^{\max}$ and $\dot{\mathbf{q}}_*^{\min}$, respectively. Together, the left $* = l$ and the right $* = r$ arms cooperatively solve the optimization problem (13) under the state and input constraints by their joint velocity inputs

$$\dot{\mathbf{q}}_* = -\frac{1}{\alpha_*} \left[\nabla_{\mathbf{q}_*} V + \nabla_{\mathbf{q}_*} \psi(\mathbf{q}_l, \mathbf{q}_r) \right],$$

where $\nabla_{\mathbf{q}_*} \psi(\mathbf{q}_l, \mathbf{q}_r)$ are the gradients of the penalty function $\psi(\mathbf{q}_l, \mathbf{q}_r)$ with respect to \mathbf{q}_* .

V. EXPERIMENTAL RESULTS

This section comparatively evaluates the proposed control with two benchmark controls via experiments on a real-robot platform. The experimental setup includes a pair of Universal Robots UR3/UR3e manipulators, as shown in Figure 2. The task of the dual-arm cooperation system is to grasp the target object, a 15 cm×15 cm×15 cm cubic orange box of weight 1.6 kg, without fixtures and transport it from the original pose to the target pose while passing 3 waypoints. Two customized bowl-shaped parts with silicone covers are mounted to the flanges of both arms to prevent them from over-squeezing the target object. The interaction wrenches between the end effectors of the two arms and their manipulated object are measured by their built-in or externally mounted Robotiq FT-300 force/torque sensors. On the wrist of each arm, an Intel RealSense D435 camera captures the four corner points of the AprilTag marker from the 36h11 family mounted on the wrist of the other arm at 30 Hz. The coordinates of the corner points on the image planes of the cameras serve as the image features for IBVS. The controls of the UR3/UR3e arms at 125 Hz/500 Hz are implemented in C++ programs that run on a single Ubuntu machine. The communications between the two manipulators and their host machine use the Robot Operating System. Because of the errors of the manipulators'

Table I
THE LEFT AND THE RIGHT ARMS' WORKSPACES IN METERS.

	arms	x -coordinate	y -coordinate	z -coordinate
left	min	-0.4375	-0.0083	-0.3497
	max	+0.4394	+0.5788	+0.6389
right	min	-0.4394	+0.1289	-0.3497
	max	+0.4375	+0.7408	+0.6389

kinematics and joint angle measurements, a motion capture system, OptiTrack V120:Trio, measures and records the end-effector poses of both manipulators at 120 Hz to compare the performances of the three controllers quantitatively.

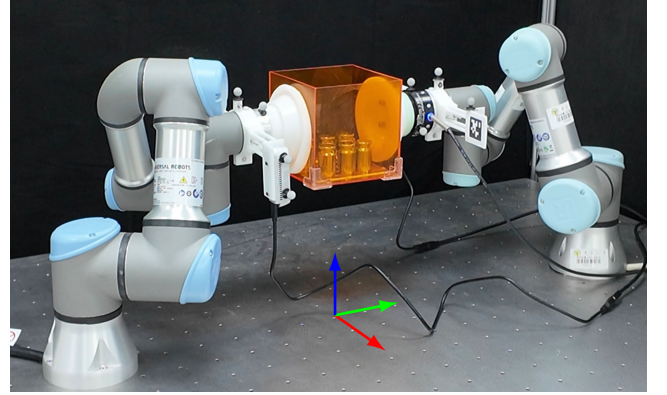


Figure 2. The experimental setup includes two Universal Robots UR3/UR3e manipulators. Both arms equip elastic tools on their flanges to cooperatively grasp a cubic box payload via frictional contacts. The camera mounted on the wrist of each arm captures the image features of the fiducial marker mounted on the wrist of the other arm.

Three comparative experiments investigate the effectiveness of the proposed control in pose synchronization (5) and IBVS enhancement (10). Specifically, the manipulator pair moves between the waypoints in the three experiments:

- exp1*: with no synchronization and no IBVS enhancement.
- exp2*: with synchronization but no IBVS enhancement.
- exp3*: with both synchronization and IBVS enhancement.

In each experiment, the left and the right arms locate their bases at (0, -0.44, 0) m and (0, 0.44, 0) m and start their joint coordinates with (80°, -70°, 130°, 120°, -35°, -35°, 0°) and (15°, -105°, -135°, 60°, 30°, 0°), respectively. Their target poses coincide with their initial poses. By the Monte Carlo algorithm, the maximum and minimum coordinates that the two manipulators' end effectors can reach are listed in Table I. Accounting for the limited workspaces, the two manipulators pick their waypoints other than their original poses as per their manipulated object. The first waypoint of the object has the position coordinates (0.23, -0.03, 0) m and the roll-pitch-yaw angles ($\frac{\pi}{10}$, $-\frac{\pi}{18}$, 0) rad. The second waypoint of the target has the position coordinate (-0.03, 0.01, 0) m and the roll-pitch-yaw angles ($-\frac{\pi}{12}$, $\frac{\pi}{12}$, 0) rad.

Figure 3 plots the Cartesian paths and the orientations at the waypoints of the two arms' end effectors in the experiments. The colors of the paths change with time as indicated in the color bar, and the coordinate frames at the waypoints mark

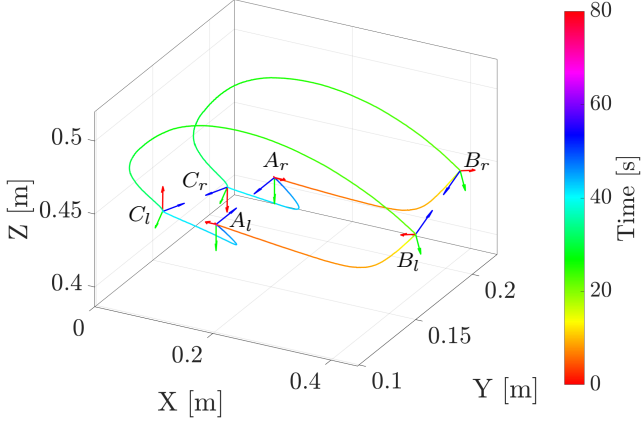


Figure 3. The Cartesian paths and the orientations at the waypoints of the left and the right arms' end effectors in the experiments. The target poses of both arms coincide with their initial poses.

the end-effector orientations of both arms. The left $* = l$ and the right $* = r$ arms start with their initial poses at the waypoints A_* , move towards the waypoints B_* and C_* , and back to the waypoints A_* with the same poses as in the beginning. One can roughly check that the relative poses between the two arms' end effectors remain nearly invariant during the movements, especially at the waypoints.

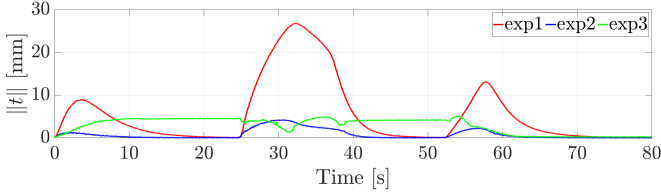


Figure 4. The position errors between the end effectors of the left and the right manipulators during the three experiments. The end-effector positions of both arms are calculated by their kinematics and joint angle measurements.

Using the kinematics and joint angle measurements of both arms, Figure 4 demonstrates the position errors between their end effectors during the three experiments. One can see that the maximum position error appears in the experiment *exp1*, reaching 26 mm at about the 32 s. By contrast, the position errors in the experiments *exp2* and *exp3* remain lower than 5 mm for all time. They thus confirm that the pose synchronization control (5) contributes to reducing the position errors between the two arms. Note that, in both experiments *exp1* and *exp2*, the position errors grow with the movement speeds of both arms and reduce to zero when arriving at their waypoints at the 25 s and the 52 s. However, the position error in the experiment *exp3* stays around 5 mm. This is primarily because the statistical position error is not the true value when there exist errors in the kinematics and joint angle measurements of both arms. Based on the inaccurate position measurements, the conventional controls coordinate both arms with intrinsic position errors. By contrast, the proposed control uses IBVS to correct the position errors, thereby enhancing the cooperation of both manipulators.

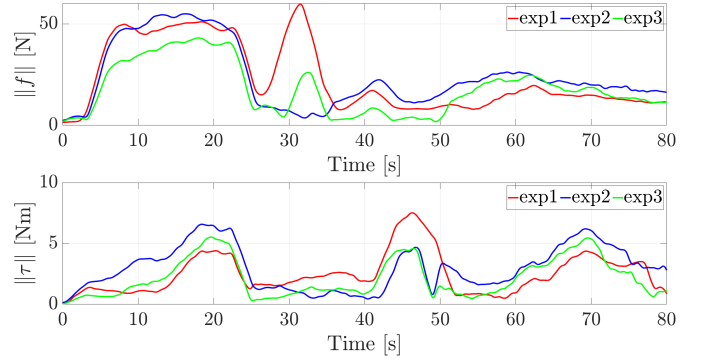


Figure 5. The internal forces (the top subplot) and the internal torques (the bottom subplot) between the end effectors of the left and the right arms during the three experiments. The interaction forces and torques are measured by the built-in or externally mounted Robotiq FT-300 force/torque sensors.

By low-pass filtering the measurements of the force/torque sensors, Figure 5 compares the internal forces and torques between the end effectors of the left and the right manipulators in the three experiments. One can see that the profiles of both the internal forces in the top subplot and the internal torques in the bottom subplot look similar in all three experiments, especially before the 30 s and after the 60 s. Nevertheless, compared to the experiments *exp2* and *exp3*, the experiment *exp1* encounters the greatest internal forces (60 N) and torques (7.5 Nm) at the 35 s and the 52 s, respectively. The maximum internal forces and torques in the experiment *exp2* are about 58 N and 7 Nm, while the maximum internal forces and torques in the experiment *exp3* are about 42 N and 5.5 Nm. They substantiate that the pose synchronization control (5) and the IBVS enhancement (10) both contribute to reducing the internal forces and torques during the task execution.

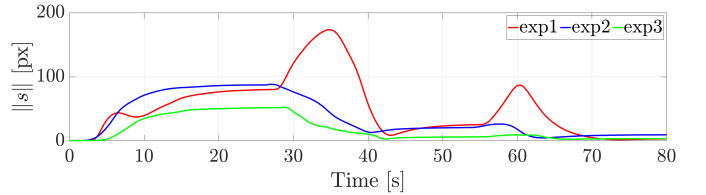


Figure 6. The errors of the image features from their desired values in the three experiments. The values of the image features are measured by the cameras mounted on the wrists of the left and the right manipulators.

Figure 6 depicts the errors of the image features that are captured by the two arms' wrist-mounted cameras from their desired values in all three experiments. One can find that the image feature error in the experiment *exp1* is significantly larger than that in the experiments *exp2* and *exp3* from the 28 s to the 42 s and from the 55 s to the 70 s. The maximum image feature errors in the experiments *exp1*, *exp2* and *exp3* are 175 px, 90 px and 50 px, respectively. Throughout the task execution, the image feature error in the experiment *exp3* maintains the smallest compared to that in the other two experiments. Because the image feature errors indicate the pose errors, they thus substantiate that the pose synchronization control (5) and the IBVS enhancement (10) both reduce the

Table II
THE MAXIMUM AND THE MEAN FROBENIUS NORMS OF THE ERROR
MATRICES $\tilde{\mathbf{T}}$ IN THE THREE EXPERIMENTS.

experiments	$\max(\ \tilde{\mathbf{T}}\ _F)$	$\text{mean}(\ \tilde{\mathbf{T}}\ _F)$
<i>exp1</i>	2.2316	2.0859
<i>exp2</i>	2.2297	2.0780
<i>exp3</i>	2.2280	2.0672

pose errors between the end effectors of the left and the right manipulators.

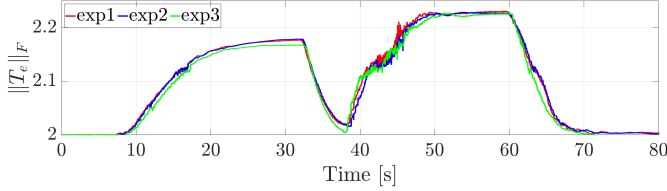


Figure 7. The Frobenius norms of the error matrices $\tilde{\mathbf{T}}$ measured by the motion capture system in the three experiments.

With the motion capture system, Figure 7 plots the Frobenius norms of the error matrices $\tilde{\mathbf{T}}$ measured in all three experiments. By fixing 4 non-coplanar markers on the last link of each manipulator, the position coordinates of all 8 markers in the frame of the motion capture system reflect the pose errors between the end effectors of the left $* = l$ and the right $* = r$ manipulators. Specifically, let the homogeneous position coordinates of the markers $i = 1, 2, 3, 4$ on the arms $*$ in the frame of the motion capture system be χ_{*i} . There then exists a unique homogeneous matrix \mathbf{T} such that

$$\mathbf{T} \begin{bmatrix} \chi_{l1} & \chi_{l2} & \chi_{l3} & \chi_{l4} \end{bmatrix} = \begin{bmatrix} \chi_{r1} & \chi_{r2} & \chi_{r3} & \chi_{r4} \end{bmatrix}.$$

The error matrix $\tilde{\mathbf{T}} = \mathbf{T}\bar{\mathbf{T}}^{-1}$ of \mathbf{T} from its initial value $\bar{\mathbf{T}}$ implies that pose error between the end effectors of the two manipulators. From Figure 7, one can see that the Frobenius norm of $\tilde{\mathbf{T}}$ in the experiment *exp3* stays the smallest most of the time compared to that in the experiments *exp1* and *exp2*. Quantitatively, Table II evaluates that the maximum and the mean of the Frobenius norm of $\tilde{\mathbf{T}}$ in the experiment *exp3* both are the smallest among all three experiments. Together, they verify that both the pose synchronization control (5) and the IBVS enhancement control (10) contribute to reducing the pose errors between the end effectors of the two arms.

To sum up, Figures 5-7 and Table II all illustrate that, compared to the two benchmark controls, the proposed control with both pose synchronization (5) and IBVS enhancement (10) obtains the smallest pose errors and internal wrenches in the experiments. Figure 4 indicates that the conventional controls lead to the missynchronization of the manipulators' end effectors in the presence of systematic errors in their kinematics and joint angle measurements. The IBVS for cooperation enhancement is thus needed to handle the problem.

VI. CONCLUSION

This paper has developed an IBVS approach for enhancing the cooperation of dual-arm manipulation. By coordinating the

two arms with their kinematics and joint angle measurements, the conventional controls lead to significant end-effector pose synchronization errors of the dual-arm system when systematic errors exist. In contrast, the proposed control can mitigate the pose synchronization errors because the IBVS enhancement is robust to the systematic errors in the manipulators' kinematics and joint coordinate measurements. Technically, the paper has modeled the kinematics of a dual-arm manipulation system, has tailored the interaction matrix to the dual-arm system, has designed the joint velocity control inputs to the two arms with rigorous stability proof, and has discussed the steady-state errors and the handling of the state and input constraints. Future studies will control the interaction forces between the manipulators and their grasped objects and will coordinate them to assemble parts and components on floating bases.

REFERENCES

- [1] A. Billard and D. Kragic, "Trends and challenges in robot manipulation," *Science*, vol. 364, no. 6446, p. eaat8414, 2019.
- [2] D. Rakita, B. Mutlu, M. Gleicher, and L. M. Hiatt, "Shared control-based bimanual robot manipulation," *Science Robotics*, vol. 4, no. 30, p. eaaw0955, 2019.
- [3] F. Krebs and T. Asfour, "A bimanual manipulation taxonomy," *IEEE Robotics and Automation Letters*, vol. 7, no. 4, pp. 11 031–11 038, 2022.
- [4] F. Caccavale and M. Uchiyama, "Cooperative manipulation," in *Springer Handbook of Robotics*, B. Siciliano and O. Khatib, Eds. Berlin, Germany: Springer, 2016, pp. 989–1006.
- [5] P. Chiacchio, S. Chiaverini, and B. Siciliano, "Direct and inverse kinematics for coordinated motion tasks of a two-manipulator system," *Journal of Dynamic Systems, Measurement, and Control*, vol. 118, no. 4, pp. 691–697, 12 1996.
- [6] P. B. g. Dohmann and S. Hirche, "Distributed control for cooperative manipulation with event-triggered communication," *IEEE Transactions on Robotics*, vol. 36, no. 4, pp. 1038–1052, 2020.
- [7] E. Shahriari, S. A. B. Birjandi, and S. Haddadin, "Passivity-based adaptive force-impedance control for modular multi-manual object manipulation," *IEEE Robotics and Automation Letters*, vol. 7, no. 2, pp. 2194–2201, 2022.
- [8] I. D. Walker, R. A. Freeman, and S. I. Marcus, "Analysis of motion and internal loading of objects grasped by multiple cooperating manipulators," *The International Journal of Robotics Research*, vol. 10, no. 4, pp. 396–409, 1991.
- [9] Y. He, M. Wu, and S. Liu, "A cooperative optimization strategy for distributed multi-robot manipulation with obstacle avoidance and internal performance maximization," *Mechatronics*, vol. 76, p. 102560, 2021.
- [10] N. Dehio, J. Smith, D. L. Wigand, P. Mohammadi, M. Mistry, and J. J. Steil, "Enabling impedance-based physical human–multi-robot collaboration: Experiments with four torque-controlled manipulators," *The International Journal of Robotics Research*, vol. 41, no. 1, pp. 68–84, 2022.
- [11] Y. Zhang, X. Zhao, B. Tao, and H. Ding, "Multi-objective synchronization control for dual-robot interactive cooperation using nonlinear model predictive policy," *IEEE Transactions on Industrial Electronics*, vol. 70, no. 1, pp. 582–593, 2023.
- [12] D. Ortenzi, R. Muthusamy, A. Freddi, A. Monteriù, and V. Kyrki, "Dual-arm cooperative manipulation under joint limit constraints," *Robotics and Autonomous Systems*, vol. 99, pp. 110–120, 2018.
- [13] S. Tarbouriech, B. Navarro, P. Fraisse, A. Crosnier, A. Cherubini, and D. Sallé, "Dual-arm relative tasks performance using sparse kinematic control," in *2018 IEEE/RSJ International Conference on Intelligent Robots and Systems (IROS)*, 2018, pp. 6003–6009.
- [14] M. Costanzo, G. De Maria, and C. Natale, "Tactile feedback enabling in-hand pivoting and internal force control for dual-arm cooperative object carrying," *IEEE Robotics and Automation Letters*, vol. 7, no. 4, pp. 11 466–11 473, 2022.
- [15] Y. Gombo, A. Tiwari, M. Safwat, H. Chang, and S. Devasia, "Delayed self-reinforcement to reduce deformation during decentralized flexible-object transport," *IEEE Transactions on Robotics*, vol. 40, pp. 999–1018, 2024.

- [16] N. Vahrenkamp, C. Böge, K. Welke, T. Asfour, J. Walter, and R. Dillmann, "Visual servoing for dual arm motions on a humanoid robot," in *2009 9th IEEE-RAS International Conference on Humanoid Robots*, 2009, pp. 208–214.
- [17] J. Qu, F. Zhang, Y. Fu, and S. Guo, "Multi-cameras visual servoing for dual-arm coordinated manipulation," *Robotica*, vol. 35, no. 11, p. 2218–2237, 2017.
- [18] R. Mebarki, V. Lippiello, and B. Siciliano, "Toward image-based visual servoing for cooperative aerial manipulation," in *2015 IEEE International Conference on Robotics and Automation (ICRA)*, 2015, pp. 6074–6080.
- [19] F. Basile, F. Caccavale, P. Chiacchio, J. Coppola, and A. Marino, "A decentralized kinematic control architecture for collaborative and cooperative multi-arm systems," *Mechatronics*, vol. 23, no. 8, pp. 1100–1112, 2013.
- [20] T. Hatanaka, Y. Igarashi, M. Fujita, and M. W. Spong, "Passivity-based pose synchronization in three dimensions," *IEEE Transactions on Automatic Control*, vol. 57, no. 2, pp. 360–375, 2012.
- [21] F. Aghili, "Adaptive control of manipulators forming closed kinematic chain with inaccurate kinematic model," *IEEE/ASME Transactions on Mechatronics*, vol. 18, no. 5, pp. 1544–1554, 2013.
- [22] F. Chaumette and S. Hutchinson, "Visual servo control. i. basic approaches," *IEEE Robotics & Automation Magazine*, vol. 13, no. 4, pp. 82–90, 2006.